

Continuous drive friction welding of AISI 8630 low-alloy steel: experimental investigations on microstructure evolution and mechanical properties

Amborish Banerjee¹

Advanced Forming Research Centre (AFRC), University of Strathclyde

85 Inchinnan Drive, Inchinnan, Renfrewshire, PA 4 9LJ, UK

amborish.banerjee@strath.ac.uk, amborishbanerjee1205@gmail.com

Michail Ntovas

Advanced Forming Research Centre (AFRC), University of Strathclyde

85 Inchinnan Drive, Inchinnan, Renfrewshire, PA 4 9LJ, UK

dovas13@gmail.com

Laurie Da Silva

Advanced Forming Research Centre (AFRC), University of Strathclyde

85 Inchinnan Drive, Inchinnan, Renfrewshire, PA 4 9LJ, UK

laurie.da-silva@strath.ac.uk

Ryan O' Neill

Advanced Forming Research Centre (AFRC), University of Strathclyde

85 Inchinnan Drive, Inchinnan, Renfrewshire, PA 4 9LJ, UK

r.o-neill@strath.ac.uk

Salaheddin Rahimi

Advanced Forming Research Centre (AFRC), University of Strathclyde

85 Inchinnan Drive, Inchinnan, Renfrewshire, PA 4 9LJ, UK

salah.rahimi@strath.ac.uk

ABSTRACT

Continuous drive friction welding (CDW) is a state-of-the-art solid-state welding technology for joining

metallic components used in aerospace, oil and gas and power generation industries. This study summarises

the results of mechanical and microstructural investigations on a modified AISI-8630 steel subjected to CDW.

¹ Email id: amborish.banerjee@strath.ac.uk, amborishbanerjee1205@gmail.com, Telephone: +447594660185

34 *The effects of welding process parameters, including rotational speed, friction and forge forces, during CDW*
35 *were explored to determine an optimum welding condition. The mechanical properties of the weld, and*
36 *microstructural characteristics across different regions of the weld were measured and examined. The*
37 *microstructure characterisation results suggest that the weld zone (WZ) experiences temperatures above*
38 *the A_{c3} and the thermo-mechanically affected zone (TMAZ) experiences temperatures between A_{c1} and A_{c3}*
39 *of the material. Investigations with electron backscatter diffraction (EBSD) demonstrated the occurrence of*
40 *strain induced dynamic recrystallisation in the weld. The weld demonstrated higher yield and ultimate*
41 *tensile strengths at the expense of ductility and hardening capacity compared to the base metal (BM). The*
42 *strain hardening profiles of the welds exhibited a dual-slope characteristic, an indication of different levels*
43 *of plastic deformation experienced by the constituent phases (i.e., martensite, bainite and ferrite) present*
44 *in the microstructure. The maximum strength-to-ductility combination and static toughness values were*
45 *obtained for the weld produced under the highest rotational speed, maximum friction force and an*
46 *intermediate forge force of 1200-1400 rpm, 375-425 kN and 600-650 kN, respectively.*

47 **Keywords:** Continuous drive friction welding, strain-induced dynamic recrystallisation, welding
48 parameters, mechanical properties, strain hardening, fracture

49 **1. INTRODUCTION**

50 Low carbon-low alloy steels are extensively used in crude oil and natural gas
51 transportation due to their superior mechanical properties. Particularly, in the offshore
52 industry where the material is exposed to critical environmental conditions, low-alloy
53 steels are mostly used in the form of forged components for subsea applications. AISI
54 8630 low-alloy high strength steel, due to its better weldability and optimum strength-
55 ductility combination has been widely used in oil excavation (e.g., drilling) applications
56 including block valves, hangers and connectors for oil patches [1]. These pipelines and
57 structural components are joined together by conventional welding techniques that are

58 prone to different modes of failure [2]. The microstructural heterogeneity of the weld
59 makes it more susceptible to crack initiation and propagation. In general, the weld
60 components are typically used under enormous service loads and exposed to critical
61 conditions (e.g., high pressure, turbulent flow). Therefore, understanding the structural
62 integrity of welds is of significant importance for a robust design of hydraulic piping
63 systems.

64 Rotary friction welding (RFW) is a solid-state joining process where two parts are
65 joined under severe shear deformation at elevated temperatures resulted from frictional
66 heat generated by the relative rotation of the faying surfaces under the application of an
67 axial force. For RFW, one of the weldment parts is rotated to a predefined rotational
68 speed, while the other side is fixed on a stationary axis and pushed against the rotating
69 side with an applied force. This leads to friction between the interface of the two
70 weldment parts and increases the temperature resulting in the softening of the material
71 and finally the weld. The weld parameters such as friction and forge forces, rotational
72 speed and friction time play major roles in altering the mechanical properties of the final
73 weld [3]. The RFW technique is classified into two categories of CDW and inertia friction
74 welding (IFW). In CDW, the rotating part is directly connected to a motor, turning at a
75 constant rpm during welding, while in IFW the rotating component is attached to a
76 flywheel which stores the kinetic energy that is transformed into frictional heat during
77 the welding process [4]. The benefits of RFW over the conventional welding methods are
78 that (a) it is a solid-state joining process and thus the formation of solidification cracks,
79 pores, and other associated defects are reduced, (b) there is no requirement for welding

80 flux, filler material or shielding, (c) the localised deformation and high temperature at the
81 weld interface, leads to the formation of recrystallised grains, resulting in better
82 mechanical properties compared to the BM, etc. [4].

83 Udayakumar et al. [5] investigated the mechanical properties of dual-phase (i.e.,
84 ferritic-austenitic) duplex stainless steel welds produced by CDW under variable process
85 parameters (i.e., friction pressure, upset pressure, burn-off length and rotational speed).

86 The study showed an increase in the tensile strength and hardness of the welded
87 materials that were correlated with the ferrite grain size and the volume fraction of the
88 austenite and ferrite phase. Hazra et al. [6] conducted CDW on austenitic stainless steel
89 while varying the forge force and found no significant effect on the weld's tensile
90 strength. The weld demonstrated inferior strength than that of the BM and most failures
91 were observed in the weld zone. Selvamani et al. [7] observed that the rotational speed
92 of the weld had a greater effect on the ultimate tensile strength compared to the forge
93 and friction forces during CDW of AISI 1035 steel. Sahin [8] reported an increase in the
94 tensile strength of AISI304 stainless steel welds made by CDW, with increasing friction
95 time and force up to an optimum value beyond which an adverse effect was observed. It
96 was concluded that the application of a higher friction force was creating these effects.

97 From the literature survey, it can be concluded that several research works on the
98 CDW of different grades of steel have been reported. However, limited investigations
99 have been conducted on the CDW of AISI 8630 material. This study presents the results
100 of an investigation on the effect of three critical process parameters i.e. rotational speed,
101 friction force and forge force on the mechanical properties of the weld. The evolution of

102 microstructure during CDW is examined and correlated with the mechanical properties
103 to establish the structure-property relationships.

104 **2. MATERIAL AND EXPERIMENTAL PROCEDURES**

105 AISI 8630 steel with the nominal chemical composition of 0.3C-0.96Cr-0.9Mn-
106 0.81Ni-0.4Mo-0.3Si-0.16Cr-0.02Al-0.007P-0.006S-0.004V and balanced Fe (in wt.%) was
107 used in these investigations. The as-received material was hardened at 860 °C for 3 hours
108 and subsequently tempered at 680 °C for 6.5 hours followed by air cooling to room
109 temperature. The material was received in tubular form with 150 mm length and outer
110 and inner diameters of 80 mm and 40 mm, respectively. The welding between these two
111 mating surfaces was carried out by the CDW process using a 125-ton MTI built RFW
112 machine. For the welding, one tubular part was clamped to the rotating spindle and the
113 second tubular part was stationary on the fixture. This fixture applied the desired force in
114 the axial direction for the forging stage of the process. For this study, the effects of three
115 parameters including rotational speed, friction force, and forge force were explored to
116 determine the optimum process parameters. To maintain the confidentiality of the
117 proprietary information, instead of the precise welding process parameters, a range
118 (scaled parameter) is provided for each (Table 1). A macrograph of a typical weld joint
119 highlighting the flash generated during CDW and the fixture and the spindle side, is shown
120 in Fig. 1.

121 For the post-weld metallurgical investigations, samples were extracted from the
122 weld cross-section along the axis of the welded tubular parts. The metallographic samples
123 were ground and polished to a mirror finished condition as per the ASTM E3-11 standard

124 [9]. The mirror-finished samples were then etched using 2% Nital followed by
125 microstructure examination using a Leica DM6000 M optical light microscope (OM) and a
126 FEI Quanta™ 250 field emission gun (FEG) scanning electron microscope (SEM) equipped
127 with a Nordlys II detector for electron backscatter diffraction (EBSD) analysis.

128 For EBSD acquisitions, samples were cut from the optimum weld joint and
129 metallographically prepared to a mirror finished condition followed by vibratory polishing
130 for ≈ 12 hours using a colloidal silica suspension. For each sample, an EBSD scan was
131 carried out over an area of $100 \times 100 \mu\text{m}^2$ with a step size of $0.2 \mu\text{m}$ at an accelerating
132 voltage of 20kV. The obtained maps were post-processed using HKL-channel 5 software
133 to investigate the grain size distributions and misorientation profiles.

134 Vickers microhardness measurements were conducted on the weld cross-sections
135 covering different regions of the welds by applying 0.2 kgf load with a dwell time of 12
136 seconds. Microhardness contour plots were then constructed from the measured data
137 for each weld sample with 0.5 mm and 1.5 mm spacing across the weld and along the
138 thickness, respectively. Uniaxial tensile tests were conducted on the welds according to
139 ASTM E-8M standard [10] under a constant strain rate of 0.00025/s at ambient
140 temperature. Tensile specimens with 20 mm gauge length and 6 mm gauge diameter
141 were extracted across the axial direction (or longitudinal direction) of the weld joints with
142 the weld-zone located in the middle of the gauge section. It is worth mentioning here that
143 the gauge section consisted of all the different weld regimes i.e. WZ, TMAZ and HAZ in
144 addition to that of the BM. The experiments were performed using a screw-driven Zwick
145 Z250/SW5A testing machine calibrated with a 250-kN load cell. An extensometer with a

146 30 mm gauge length was used to measure the displacement during tensile tests. Three
147 specimens were tested for each condition to ensure repeatability and consistency in the
148 data.

149 The fracture surfaces of the failed tensile specimens were examined under SEM
150 to understand the effect of microstructural features on the final fracture. The size and
151 density of the dimples observed on the fracture surface were measured using ImageJ
152 image analysis software. More than 100 individual dimples, spread throughout the
153 fracture surface, were identified and their characteristics (i.e. size and density) were
154 measured using a procedure identical to the equi-circular diameter (ECD) method. The
155 slant regions of the fracture surface were not considered for measurement to minimise
156 uncertainty in the reported results.

157 **3. RESULTS AND DISCUSSION**

158 **3.1. Microstructure characterisation**

159 The microstructure appearances of the BM and different regions of the weld are
160 shown in Fig. 2. The cross-sectional macrograph of the weld shown in Fig. 2a
161 demonstrates the WZ, TMAZ, HAZ and the flash (the extruded material) during the CDW
162 from the weld interfaces. The TMAZ is the area adjacent to the WZ where the
163 temperature is comparatively lower, and the HAZ is a region between the TMAZ and BM.
164 The WZ and TMAZ were comparatively much narrower than the HAZ. The microstructure
165 of the BM consisted of bainite and ferrite in the matrix along with carbide precipitates, as
166 shown in Fig. 2b. Different morphologies of bainite were observed including lower bainite,
167 upper bainite, granular bainite and plate-like bainite. The microstructure of the WZ (refer

168 Fig. 2c, d) is dominated by martensite ($\approx 80\%$) with a small fraction of bainite ($\approx 15\%$) and
169 retained austenite (RA) ($\approx 5\%$). It is important to mention here that the provided volume
170 fraction of the available phases is purely quantitative based. Fig. 2c depicts the presence
171 of RA in the WZ. This implies that the temperature in the WZ may have approached the
172 A_{c3} temperature during welding. The A_{c1} and A_{c3} temperatures for the AISI-8630 steel
173 used in this study were calculated to be $\sim 730 \pm 20$ °C and 772 ± 15 °C, respectively. This
174 suggests that the temperature in the WZ during the welding process reached ~ 772 °C
175 where the majority of the microstructure was transformed to austenite with a small
176 fraction of remaining ferrite. This was then subjected to severe shear deformation
177 induced by the welding process. Post IFW fast cooling from this temperature resulted in
178 a transformation of the austenite to martensite and bainite, where traces of RA can also
179 be observed in the microstructure. The microstructure of the TMAZ, shown in Fig. 2e
180 demonstrates the presence of martensite, bainite and ferrite which signifies that the
181 temperature experienced in this zone was slightly lower than that of the WZ (i.e., between
182 A_{c1} and A_{c3}). The increase in the fraction of bainite is an indication of the lower
183 temperature reached during CDW and the slower cooling rate of the TMAZ compared to
184 the WZ. The HAZ exhibited a similar microstructure (refer Fig. 2f) as that of the BM,
185 signifying that the temperature experienced in the HAZ was below A_{c1} . Similar studies on
186 correlating the changes in the microstructure with the likely peak temperature attained
187 within different weld regions in micro-alloyed steel during friction stir welding have been
188 reported before by Rahimi et al. and Baker et al. [11, 12].

189 EBSD maps across different regions of the CD9 weld were carried out to study the
190 microstructure morphology and the possible evolutionary mechanisms during welding.
191 The orientation image map (OIM) with inverse pole figure (IPF) colouring with respect to
192 the axial direction (AD) and the plots of misorientation angle distributions for each of the
193 weld zones are shown in Fig. 3. The BM consists of both coarse grains and lath-type
194 structures with an average size of $\approx 11.2 \mu\text{m}$ (Fig. 3a,). The corresponding misorientation
195 distribution shown in Fig. 3b exhibits the presence of $\approx 56\%$ low angle grain boundaries
196 (LAGB) and $\approx 44\%$ high angle grain boundaries (HAGB). Note that the threshold angles of
197 XX and YY were considered for the classification of LAGB and HAGB, respectively.

198 The microstructures of the WZ and TMAZ, in comparison to the BM, were more
199 refined with a higher fraction of LAGBs which is an indication of subgrains formed via
200 dislocation cell structures. From Fig. 3c and e, the average size of the randomly oriented
201 grains, as well as, laths in the WZ and TMAZ were calculated to be $\approx 7.5 \mu\text{m}$ (Fig. 3c) and
202 $10 \mu\text{m}$ (Fig. 3e) μm , respectively. The presence of refined grains in the WZ can be due to
203 the occurrence of dynamic recrystallisation at high temperatures and under severe plastic
204 deformation at the interface of the weld. This means that the frictional heat leads to the
205 transformation of the BM microstructure to austenite and then the transformed
206 austenite undergoes shear deformation during IFW. This results in strain-induced
207 dynamic recrystallisation and the formation of fine austenite grains, which on fast cooling
208 restrict the growth of laths and leads to a finer microstructure. From Fig. 3d, the fractions
209 of LAGBs and HAGBs in the WZ were calculated as ≈ 60 and 40% . While the plot of
210 misorientation angle distributions for the TMAZ (see Fig. 3f) shows 63% and 37% fractions

211 for LAGBs and HAGBs, respectively, the average grain/lath size is larger than that of the
212 WZ. According to Ma et al. [13], the lower fraction of LAGBs in the WZ is due to the
213 gradients in the plastic deformation, temperature and shear strain rate experienced by
214 the material between the centre of the WZ and the BM during the CDW. It is well
215 understood that the strain rate and temperature experienced by the material in the WZ
216 are relatively higher than that of the TMAZ [1]. Therefore, the temperature and the strain
217 energy in the WZ overcomes the threshold for recrystallisation, resulting in strain-induced
218 dynamic recrystallisation while some of the strain energy still exists in the microstructure
219 in form of dislocation cell structures manifested as LAGBs. In the HAZ (see Fig. 3g), the
220 grains were coarser than that of the WZ and TMAZ with an average grain size $\approx 10.5 \mu\text{m}$,
221 which was similar to that of the BM ($11.2 \mu\text{m}$). This small decrease in the grain size in the
222 HAZ is mainly because of the carbide precipitates that hinders the grain growth.
223 Moreover, the fraction of LAGBs and HAGBs were calculated as ≈ 55 and 45% ,
224 respectively, which are similar to those of the BM (Fig. 3b and h).

225 **3.2. Tensile properties of the weld**

226 The flow behaviour of the tensile specimens, taken from different welding
227 conditions was investigated by conducting tensile tests at room temperature. The results
228 were then compared with that of the BM material. The engineering stress-strain curves
229 corresponding to different weld samples are shown in Fig. 4a where they all exhibit
230 discontinuous yielding (i.e., double yielding) and drastic strain hardening behaviour. This
231 phenomenon is shown in the inset of Fig. 4a in the form of two inflexion points and was
232 found to occur for all the tested specimens. The uniform and total elongation values

233 obtained from the stress-strain curves show that the maximum total elongations (TE)
234 were exhibited by the CD7 and CD9 weld conditions (see Fig. 4b) which corresponds to
235 the welds produced under the highest rotational speed (1200-1400 rpm). The occurrence
236 of necking followed by final fracture was noticed in a region between the HAZ and BM for
237 all the tested specimens, which is an indication of the higher strength of the weld zone.
238 The formation of Lüders bands that are associated with the formation of the Cottrell
239 atmosphere can be considered as the major reason for the yield point elongation (shown
240 in Fig. 4b). A Cottrell atmosphere is created by the diffusion of interstitial atoms, such as
241 carbon or nitrogen, leading to the obstruction of dislocations and is very likely to occur
242 during the welding process [14]. Significant strain hardening was observed in all
243 specimens irrespective of the welding condition until the ultimate tensile strength (UTS)
244 was reached. A uniform elongation (UE) of 4.7-6.6% was recorded for these tests
245 whereas, the maximum elongation was that of the CD9 specimen. The fracture surface of
246 the tested specimens exhibited cup-cone failure which is an indication of ductile fracture.
247 The variation in the yield and UTS of the tested specimens is presented in Fig. 4c and d,
248 respectively. The maximum range of yield and UTS values were recorded for tensile
249 specimens extracted from the welds carried out at the highest rotational speeds (i.e. CD
250 7-9). The yield and UTS of the BM were 587 MPa and 751 MPa, respectively. Thus, it can
251 be concluded that a significant increase in the yield strength was obtained for the welds
252 produced under the maximum rotational speeds, whereas the increase in the UTS was
253 marginal. Meanwhile, more than 100% joint efficiency (i.e. ratio of the strength of the
254 weld to that of the BM) was achieved for all weld conditions. The effects of other process

255 parameters (i.e. friction force, forge force and friction dwell time) have been discussed in
256 detail in the following sections.

257 **3.3. Strain hardening behaviour of the welds**

258 The strain hardening rate (SHR) was calculated from the plastic regime of the true
259 stress-strain curves and smoothed using the adjacent averaging method. The SHR
260 $\left(\theta = \frac{d\sigma}{d\varepsilon}\right)$ of all the weld samples with respect to the true strain are shown in Fig. 5. The
261 SHR of the welds were significantly higher than that of the BM. The welds exhibited three
262 stages of SHR (i.e. stage II, III and IV) as a function of true plastic strain. Stage-I is not
263 presented in Fig. 5 as it corresponds to the deformation of the welded materials in the
264 elastic regime. The strain hardening behaviour depends on the dislocation density and
265 grain size of the materials and has been explained by Khodaverdizadeh et al. [15] based
266 on dislocation theory. The authors reported that for friction stir welded copper material,
267 the coarsening of the grains resulted in a decrease in the SHR, whereas a drop in the
268 dislocation density leads to an increase in the SHR of the welds. As shown in Fig. 5, an
269 initial steep increase in the SHR was evaluated which corresponds to stage II that can be
270 linked to microstructural characteristics.

271 The initial steep increase in the SHR at lower strains can be attributed to (a) the
272 high dislocation density in the ferrite-martensite interfaces, (b) internal stress generation
273 in the weld due to the post-CDW rapid cooling from the austenitic region (i.e. at or above
274 A_{c3}), and (c) the difference in the flow behaviour of the constituent microstructural
275 phases (i.e., martensite, bainite and ferrite). Once the true plastic strain exceeds $\sim 0.2\%$,
276 the curves exhibit a prompt decrease indicating the start of stage III work-hardening

277 behaviour. In this stage, dynamic recovery and dislocation annihilation occur as opposed
278 to dislocation multiplication. According to Ashrafi et al. [16], during tensile deformation,
279 a reduction in the work hardening rate of ferritic/bainitic/martensitic microstructures is
280 expected because their plastic deformation is restricted by the hard martensite phase. In
281 other words, martensite being the hardest phase will remain in the elastic state during
282 the initial stage of deformation, whereas, plastic flow will occur in the ferrite and bainite
283 matrix. Under such circumstances, the applied stress is transferred from the
284 ferrite/bainite to the martensite in the WZ and TMAZ. However, due to the change in the
285 content of the available phases in the WZ and TMAZ, the stress transfer is different and
286 thus leads to heterogeneous stress localisation [17]. In this study, as observed from the
287 microstructure (refer Fig. 4), no evidence of martensite is found in the HAZ and the BM,
288 leading to the conclusion, that both ferrite and bainite withstand the entire stress and
289 undergo deformation during the initial stages of deformation. In the WZ and TMAZ,
290 martensite is also observed in addition to ferrite and bainite. This implies that the stresses
291 accumulated in the ferrite and bainite were transferred to martensite, and at a later stage,
292 all these three phases undergo plastic deformation. For this investigation, it can be
293 concluded that stage III marks the simultaneous deformation of all the available phases
294 i.e. ferrite, bainite and martensite, which is also governed by dynamic recovery and cross-
295 slip processes [18]. Similar observations for simultaneous deformation of both ferrite and
296 martensite in stage III have been documented in other reports [18-20]. Following stage
297 III, stage IV indicates a progressive decrease in strain hardening rate as a function of true
298 strain. According to Cuddy et al. [21], the increase in the dislocation movements due to

299 the cross-slip phenomenon can be considered as the major reason for this relatively linear
300 decline in the strain hardening. The microstructures of all the weld regions (i.e. WZ, TMAZ,
301 and HAZ) and BM depicted different contents for different phases. Thus, it is expected
302 that during the deformation process, some of the phases undergo elastic deformation,
303 while other phases experience plastic deformation. This heterogeneity in the deformation
304 behaviour combined with the different yield strengths associated with the constituent
305 phases may be the cause of the observed fluctuations in the SHR curves.

306 The strain hardening exponent was evaluated to further investigate the strain
307 hardening behaviour of the welds. The strain hardening exponent is a measure of the
308 strain hardenability; typically a material with a high strain hardening exponent undergoes
309 uniform deformation in the plastic regime. The stress-strain behaviour in the plastic
310 regime during the uniform deformation stage is expressed by the Hollomon relationship
311 in Equation 2 [22].

$$312 \quad \sigma = k\varepsilon^n \quad (2)$$

313 In Equation 2, k is the coefficient of strength and n is the strain hardening
314 coefficient, σ and ε represent the true stress and true strain, respectively. The weld
315 specimens exhibited a non-linear variation in the $\ln \sigma$ versus $\ln \varepsilon$, thus demonstrating a
316 bi-linear slope in the strain hardening (see Fig. 6a) behaviour. An illustrative example of
317 the methodology followed for evaluating the n_1 and n_2 exponents (i.e., for both strain
318 hardening stages) is presented in Fig. 6b. The linear equations for the fitted curves and
319 the degree of fit (i.e. R^2) were considered when evaluating the strain hardening exponents
320 presented in Table 2. The first stage of the strain hardening curve depicts a higher strain

321 hardening exponent value (n_1) compared to the second stage (n_2). The different stages of
322 strain hardening behaviour of the weld tensile test specimens can be explained based on
323 the level of plastic deformation experienced by the constituent microstructural phases.
324 As martensite is harder than ferrite, bainite and austenite, during the onset of plastic
325 deformation, the regions dominated by ferrite and bainite phases will undergo initial
326 deformation until the threshold stress is reached, after which the plastic deformation
327 extends to martensite. The observed dual-slope in the strain hardening behaviour of the
328 weld specimens can be attributed to this heterogeneous plastic deformation behaviour
329 in these phases. The first stage of strain hardening, indicates the deformation of softer
330 phases such as austenite and ferrite, whereas, the second stage demonstrates the plastic
331 deformation in the bainite and martensite in addition to austenite and ferrite. These
332 observations are in an agreement with previous results reported on the strain hardening
333 behaviours of different types of dual-phase steels [23, 24]. Higher values of n_1 compared
334 to n_2 were evaluated for all the welds, which based on Ashby's [25] explanations, is due
335 to the pile-up of the geometrically necessary dislocations at the interfaces of the phases.
336 Moreover, the strain hardening exponents of all the welds were found to be lower than
337 those obtained for the BM. This implies a decrease in the deformability of the weld
338 specimens in the uniform plastic regime compared to the BM. This can be attributed to
339 the presence of martensite in the WZ and TMAZ of the welded specimens, which
340 ultimately leads to an increase in the strength of the weld specimens at the loss of
341 ductility. The decrease in the n values indicates similar behaviour i.e. a drop in the ductility
342 of the weld specimens compared to the BM.

343 The hardening behaviour of the welds was also evaluated by the hardening
344 capacity (H_c) based on an approach described by Afrin et al. [26] using a normalised
345 relationship expressed in Equation 3.

$$346 \quad H_c = \frac{\sigma_u}{\sigma_y} - 1 \quad (3)$$

347 In Equation 3, σ_u and σ_y represent the UTS and yield strength of the material. The
348 evaluated hardening capacity values for the welds and BM are provided in Table 2. The
349 data shows a decrease in the hardening capacity of the welded specimens compared to
350 the BM. As per Equation 2, the yield strength of a material has a substantial effect on its
351 hardening capacity, which is linked to the grain size based on the Hall-Petch relationship.
352 Hardening in the WZ and TMAZ, owing to the austenite to martensite phase
353 transformation under rapid cooling results in a significant increase in the yield strength.
354 This can be considered as a reason for the observed drop in the hardening capacity of the
355 welds.

356 **3.4. Hardness distribution in the weld**

357 The 2D microhardness contour maps of all nine welds are presented in Fig. 7. A
358 significant variation in the hardness profiles across the transverse cross-section of the
359 weld specimens was observed, regardless of the welding condition. The average hardness
360 in the WZ of the welds was measured to be in the range of 500-660 HV, and that of the
361 TMAZ was between 290-500 HV. A few spots in the WZ with significantly higher hardness
362 values were noticed in all welds. The maximum hardness values measured in the WZ of
363 all welds, which in turn, is the hardest zone for each condition, are presented in Table 3.
364 Overall, the highest hardness in the WZ was that of the CD6 weld (~716 HV), and the

365 lowest value was that of the CD8 weld (~661 HV). Note that the lowest hardness values
366 in the WZ were measured for the weld carried out under the highest rotational speed.
367 The variation in the hardness profile of the HAZ was in-between ~230 - 285 HV, which is
368 not significantly different from that of the BM (~220-230 HV). The WZ demonstrated
369 nearly a threefold increase in the hardness compared to the BM. This substantial upsurge
370 is due to the formation of predominant lath martensite in the WZ. Similar explanations
371 can be provided for the TMAZ where due to the lower martensite content and increased
372 bainite and ferrite fractions, the hardness was comparatively lower than the WZ,
373 meanwhile much higher than that of the BM. Although the variation in hardness profile
374 across the WZ and TMAZ was extensive, no evidence of macro or microcracks were
375 observed by the techniques (i.e., OM and SEM) used in this study.

376 **3.5. Effect of process parameters on the mechanical properties of the welds**

377 The variation in the process parameters applied during CDW (i.e., rotational
378 speed, friction and forge forces) play an important role in altering the mechanical
379 properties (e.g., UTS) of the welds. To evaluate the contribution of each one of these
380 process parameters, an analysis of variance (ANOVA) was carried out as per the standard
381 ANOVA procedure [27]. In this analysis, the F-variable that specifies the confidence level
382 of process parameters, and the P-variable that indicates the fraction of the total variance
383 of an individual parameter, were used. The signal to noise (S/N) ratio along with the F and
384 P variables considering the UTS as a response parameter were calculated to identify the
385 individual effects of the process parameters. The S/N ratio for different process
386 parameters is presented in Fig. 8, and a summary of the calculated values are presented

387 in Table 4. As evident, the friction force and rotational speed had substantial impacts on
388 the UTS due to the larger F-ratio. However, the rotational speed was concluded as the
389 predominant process parameter due to its highest contribution (~60%) in increasing the
390 tensile UTS. Conversely, the forge force had a negligible effect on the variation in UTS of
391 the welds. Thus, it can be concluded that an increase in the rotational speed results in a
392 higher UTS, whereas increasing the friction force above a nominal value of 325 - 375 kN,
393 drops the UTS significantly.

394 The weld produced under the CD9 condition (see Table 1) exhibited the highest
395 yield strength (~626 MPa), UTS (~755 MPa) and static toughness (~137.5 J/mm³). Also,
396 the CD9 weld exhibited the lowest hardness, which is preferred, among all the welds
397 except CD8. Thus, based on the measured mechanical properties, CD9 which was
398 produced under the highest rotational speed and friction force, and the lowest forge force
399 is considered to be the optimum weld condition.

400 **3.6. Fracture surface examination**

401 The analysis of the fracture surfaces is beneficial for understanding the effect of
402 process parameters on the weld joints and further classifying the fracture mechanisms.
403 Since the rotational speed was the most critical parameter affecting the mechanical
404 strength of the weld joints, the fracture surfaces of the tensile specimens corresponding
405 to the three different rotational speeds were examined and the results are presented in
406 Fig. 9. It is worth mentioning here that the term “weld joint” indicates the presence of all
407 the different regions i.e. WZ, TMAZ, HAZ and the BM. The microstructural features
408 observed on the fracture surface of the CD2 weld condition is shown in Fig. 9a-c. The SEM

409 macrograph showed in Fig. 9a as an inset exhibits a typical cup and cone fracture surface
410 indicating a ductile mode of failure. The cup and cone fracture indicates that the applied
411 stress during the uniaxial tensile test is not aligned with the principal stress in the sample,
412 and this leads to maximised shear stress. The SEM images in Fig. 9a-c show the presence
413 of dimples, voids along with a few micro-cracks, and spherical particles. According to Yu
414 et al. [28], the spherical particles are formed due to the fracture of the brittle precipitates
415 and thus are an indication of a brittle failure. The presence of these features on the
416 fracture surface is an indication of mixed mode (i.e. ductile - "local" brittle) failure [28].
417 The fracture surface of the tensile specimen made from CD6 and CD9 welds exhibited
418 similar features and the presence of dimples and voids, as well as brittle spherical
419 particles (refer Fig. 9d-i).

420 To further understand the correlation between the dimples and the exhibited
421 ductility of the weld parts, the morphology of the dimples was assessed in terms of their
422 average size and density. These were measured for CD2, CD6 and CD9 weld joints,
423 produced under different rotational speeds during CDW (Table 1), and the results are
424 shown in Fig. 10. The density of dimples appears to increase with an increased rotational
425 speed. The dimple density for the CD2, CD6 and CD9 welds were calculated to be $\sim 2.9 \pm$
426 0.3 , 3.0 ± 0.3 and $3.2 \pm 0.2 / \mu\text{m}^2$, respectively. The average dimple size was found to
427 decrease with increasing rotational speed for CD2 and CD6 weld conditions, however, a
428 negligible difference is observed with a further increase in the rotational speed from CD6
429 to CD9. The average dimple size was measured to be $\sim 0.76 \pm 0.1$, 0.58 ± 0.1 and $0.59 \pm$
430 $0.1 \mu\text{m}$, respectively for the CD2, CD6 and CD9 welds. Overall, an increase in the dimple

431 density is an indication of the increase in the ductility of the material [20]. This is in
432 agreement with the outcome observed for the CD9 weld condition, which exhibited the
433 highest dimple density resulting in the highest ductility among all the examined welds.

434 **4. CONCLUSIONS**

435 In this paper, the CDW of modified AISI-8630 steel using different weld parameters
436 was investigated. The mechanical properties were evaluated and the concomitant
437 changes in the microstructural features were correlated with the mechanical properties.
438 The key findings of this study are summarised as the following:

- 439 1. The microstructure of the WZ displayed the presence of predominant martensite along
440 with bainite and traces of retained austenite, whereas in the TMAZ the existence of
441 bainite, ferrite, martensite and carbide precipitates were noticed. These features were
442 correlated with the conceivable experienced temperature across the different regions of
443 the weld. It was concluded that the WZ experienced a temperature closer to the Ac_3 and
444 the TMAZ in between Ac_1 and Ac_3 .
- 445 2. The EBSD orientation maps of the welds demonstrated a gradual increase in the grain
446 size from the centre of WZ towards the HAZ. Though the microstructures of all the weld
447 regions were dominated by LAGBs, with higher fractions in the WZ and TMAZ, a slightly
448 smaller fraction of LAGBs and considerably smaller grain size was measured for the WZ
449 compared to the TMAZ. These were attributed to the variation in the level of shear strain
450 and temperature between these zones during the welding process.
- 451 3. The welds demonstrated discontinuous yielding and three stages of strain hardening
452 rate during tensile loading. An increase in the yield strength and UTS of all welds was

453 observed at the expense of a drop in ductility, compared to those of the BM. The welds
454 exhibited a substantial decline in the hardening capacity and a significant upsurge in the
455 hardness compared to the BM.

456 4. Based on the investigated mechanical properties, the weld produced under the highest
457 rotational speed (1200 - 1400 rpm), highest friction force (375 - 425 kN), and an
458 intermediate forge force (600 - 650 kN) resulted in the desired mechanical properties and
459 as such these parameters were considered as the optimum welding condition. The
460 rotational speed followed by friction force were concluded to be the most important
461 parameters affecting the mechanical properties of the welds. The forge force had a
462 negligible effect on the strength of the weld.

463 **ACKNOWLEDGMENT**

464 The authors acknowledge the Advanced Forming Research Centre (AFRC) at the
465 University of Strathclyde for providing the laboratory facilities, which receives partial
466 financial support from the UK's High-Value Manufacturing CATAPULT. The authors would
467 like to acknowledge Kornelia Kondziolka for preparing the metallurgical specimens and
468 Jacqueline Schramm for her help with the mechanical testing.

469 **FUNDING**

470 This project received funding from the Tier-I members of the Advanced Forming Research
471 Centre (AFRC) and UK's High-Value Manufacturing CATAPULT.

472

473 **REFERENCES**

- 474 [1] A. Banerjee, M. Ntovas, L. Da Silva, S. Rahimi, Effect of rotational speed and inertia on
475 the mechanical properties and microstructural evolution during inertia friction welding of
476 8630M steel, *Materials Letters* 296 (2021) 129906.
- 477 [2] S.K. Sharma, S. Maheshwari, A review on welding of high strength oil and gas pipeline
478 steels, *Journal of Natural Gas Science and Engineering* 38 (2017) 203-217.
- 479 [3] S.T. Selvamani, K. Palanikumar, K. Umanath, D. Jayaperumal, Analysis of friction
480 welding parameters on the mechanical metallurgical and chemical properties of AISI 1035
481 steel joints, *Materials & Design (1980-2015)* 65 (2015) 652-661.
- 482 [4] W. Li, A. Vairis, M. Preuss, T. Ma, Linear and rotary friction welding review,
483 *International Materials Reviews* 61(2) (2016) 71-100.
- 484 [5] T. Udayakumar, K. Raja, A. Tanksale Abhijit, P. Sathiya, Experimental investigation on
485 mechanical and metallurgical properties of super duplex stainless steel joints using
486 friction welding process, *Journal of Manufacturing Processes* 15(4) (2013) 558-571.
- 487 [6] M. Hazra, K.S. Rao, G.M. Reddy, Friction welding of a nickel free high nitrogen steel:
488 influence of forge force on microstructure, mechanical properties and pitting corrosion
489 resistance, *Journal of Materials Research and Technology* 3(1) (2014) 90-100.
- 490 [7] S.T. Selvamani, K. Palanikumar, Optimizing the friction welding parameters to attain
491 maximum tensile strength in AISI 1035 grade carbon steel rods, *Measurement* 53 (2014)
492 10-21.
- 493 [8] M. Sahin, Evaluation of the joint-interface properties of austenitic-stainless steels (AISI
494 304) joined by friction welding, *Materials & Design* 28(7) (2007) 2244-2250.
- 495 [9] P.L. Niu, W.Y. Li, D.L. Chen, Strain hardening behavior and mechanisms of friction stir
496 welded dissimilar joints of aluminum alloys, *Materials Letters* 231 (2018) 68-71.
- 497 [10] Standard Test Methods for Tension Testing of Metallic Materials [Metric].
- 498 [11] S. Rahimi, B.P. Wynne, T.N. Baker, Development of Microstructure and
499 Crystallographic Texture in a Double-Sided Friction Stir Welded Microalloyed Steel,
500 *Metallurgical and Materials Transactions A* 48(1) (2017) 362-378.
- 501 [12] T.N. Baker, S. Rahimi, B. Wei, K. He, N.A. McPherson, Evolution of Microstructure
502 During Double-Sided Friction Stir Welding of Microalloyed Steel, *Metallurgical and*
503 *Materials Transactions A* 50(6) (2019) 2748-2764.
- 504 [13] T.J. Ma, L.F. Tang, W.Y. Li, Y. Zhang, Y. Xiao, A. Vairis, Linear friction welding of a solid-
505 solution strengthened Ni-based superalloy: Microstructure evolution and mechanical
506 properties studies, *Journal of Manufacturing Processes* 34 (2018) 442-450.
- 507 [14] A.A. Kuril, G.D. Janaki Ram, S.R. Bakshi, Microstructure and mechanical properties of
508 keyhole plasma arc welded dual phase steel DP600, *Journal of Materials Processing*
509 *Technology* 270 (2019) 28-36.
- 510 [15] H. Khodaverdizadeh, A. Mahmoudi, A. Heidarzadeh, E. Nazari, Effect of friction stir
511 welding (FSW) parameters on strain hardening behavior of pure copper joints, *Materials*
512 *& Design* 35 (2012) 330-334.
- 513 [16] H. Ashrafi, M. Shamanian, R. Emadi, N. Saeidi, Microstructure, Tensile Properties and
514 Work Hardening Behavior of GTA-Welded Dual-Phase Steels, *Journal of Materials*
515 *Engineering and Performance* 26(3) (2017) 1414-1423.

- 516 [17] Q.-h. Pang, Z.-z. Zhao, D. Tang, Microstructure and properties of hot-rolled high
517 strength bainitic steel by laser welding, *Materials & Design* 87 (2015) 363-369.
- 518 [18] T.S. Byun, I.S. Kim, Tensile properties and inhomogeneous deformation of ferrite-
519 martensite dual-phase steels, *Journal of Materials Science* 28(11) (1993) 2923-2932.
- 520 [19] A. Bag, K.K. Ray, E.S. Dwarakadasa, Influence of martensite content and morphology
521 on tensile and impact properties of high-martensite dual-phase steels, *Metallurgical and*
522 *Materials Transactions A* 30(5) (1999) 1193-1202.
- 523 [20] A. Banerjee, H. Wang, A. Brown, A. Ameri, Q. Zhu, S. Bhattacharyya, P.J. Hazell, B.G.
524 Prusty, Experimental investigation on the dynamic flow behaviour and structure-property
525 correlation of dual-phase high carbon steel at elevated temperatures, *Materials Science*
526 *and Engineering: A* 771 (2020) 138655.
- 527 [21] J. Cuddy, M. Nabil Bassim, Study of dislocation cell structures from uniaxial
528 deformation of AISI 4340 steel, *Materials Science and Engineering: A* 113 (1989) 421-429.
- 529 [22] J.H. Hollomon, Tensile deformation, *Transactions of the Metallurgical Society of AIME*
530 162 (1945) 268-289.
- 531 [23] M.M. Karimi, S. Kheirandish, Comparison of Work Hardening Behaviour of Ferritic-
532 Bainitic and Ferritic-Martensitic Dual Phase Steels, 80(2) (2009) 160-164.
- 533 [24] M.R. Akbarpour, A. Ekrami, Effect of ferrite volume fraction on work hardening
534 behavior of high bainite dual phase (DP) steels, *Materials Science and Engineering: A*
535 477(1) (2008) 306-310.
- 536 [25] M.F. Ashby, The deformation of plastically non-homogeneous materials, *The*
537 *Philosophical Magazine: A Journal of Theoretical Experimental and Applied Physics*
538 21(170) (1970) 399-424.
- 539 [26] N. Afrin, D.L. Chen, X. Cao, M. Jahazi, Strain hardening behavior of a friction stir
540 welded magnesium alloy, *Scripta Materialia* 57(11) (2007) 1004-1007.
- 541 [27] P.J. Ross, Taguchi techniques for quality engineering: loss function, orthogonal
542 experiments, parameter and tolerance design, McGraw-Hill 1988.
- 543 [28] H. Yu, Y. Wang, Fracture performance of high strength steels, aluminium and
544 magnesium alloys during plastic deformation, *MATEC Web of Conferences* 21 (2015)
545 07001.
- 546

547

Figure Captions List

548

- Fig. 1 A CDW joint of the cylindrical tubes exhibiting rotating side, fixed side and the flash formation (not to scale). The AD, RD and TD refers axial, radial and transverse direction, respectively.
- Fig. 2 SEM and OM micrographs of the BM and different regions of the weld (a) macro of the weld joint, (b) BM revealing the presence of different morphology of bainite, ferrite (F) and carbide precipitates; (c) and (d) OM and SEM micrographs of the WZ displaying the presence of bainitic ferrite (BF) , martensite (M) and retained austenite (RA); (e) SEM micrograph of the TMAZ exhibiting the presence of ferrite (F), martensite (M), bainite (B), and (f) HAZ exhibiting similar microstructure as that of BM i.e. presence of bainite, ferrite and carbides.
- Fig. 3 OIMs with IPF colouring with respect to the AD, and plots of misorientation angle distribution for different regions of the CD9 weld, (a) BM, (b) WZ, (c) TMAZ and (d) HAZ. The RD, AD and TD represents the radial, axial and transverse directions.
- Fig. 4 **Fig. 4.** (a) Engineering stress-strain curves for the welded materials and the magnified image in the inset showing the double yielding and yield point elongation during tensile tests for all samples, (b) uniform and total elongation, (c) and (d) show the variation in yield and UTS, respectively, as a function of rotation speed for different weld conditions.
- Fig. 5 The strain hardening rate versus true plastic strain of the welded samples exhibiting three different stages. Inset is the magnified plot exhibiting stage II.
- Fig. 6 (a) Strain hardening behaviour of the welds exhibiting variations of $\ln \sigma$ vs $\ln \epsilon$, (b) methodology used for evaluating the strain-hardening exponents for CD 9 weld.

- Fig. 7 Microhardness maps of all the nine CDW welds exhibiting the hardness distribution across the WZ, TMAZ, HAZ and BM.
- Fig. 8 (a) ANOVA analysis exhibiting the effects of individual process parameters on the UTS of the welds performed in this study.
- Fig. 9 Fracture morphologies of the welds following tensile experiments, (a)-(c) CD2 weld, (d)-(f) CD6 weld, (g)-(i) CD9 weld exhibiting the presence of various features such as dimples, micro-dimples, presence of spherical particles and macroscopic cracks.
- Fig. 10 Variation in the measured dimple size and density as a function of weld conditions.

550

Table Caption List

- | | |
|---------|---|
| Table 1 | The identity and ranges of RFW process parameters implemented during CDW in this study. |
| Table 2 | Strain hardening exponents and hardening capacity for the BM and the welds. |
| Table 3 | Maximum hardness values obtained for the WZ of all the welds produced under different conditions. |
| Table 4 | Summary of the calculated values for the ANOVA parameters. |

551

552 **Figures**

Figures

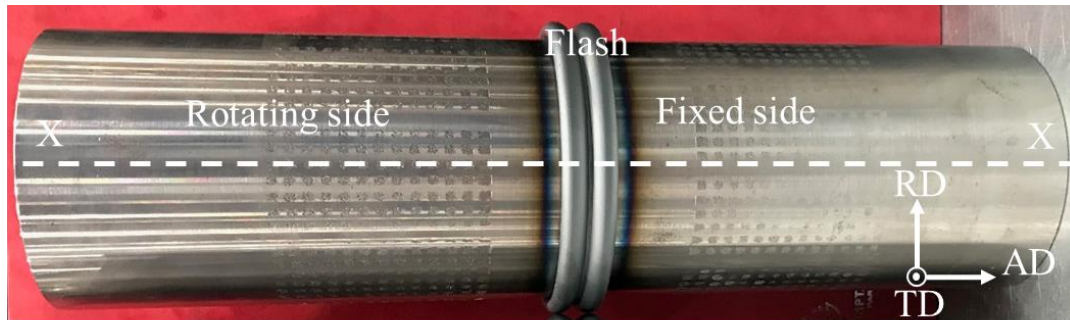


Fig. 1. A CDW joint of the cylindrical tubes exhibiting rotating side, fixed side and the flash formation (not to scale). The AD, RD and TD refers axial, radial and transverse directions, respectively.

553

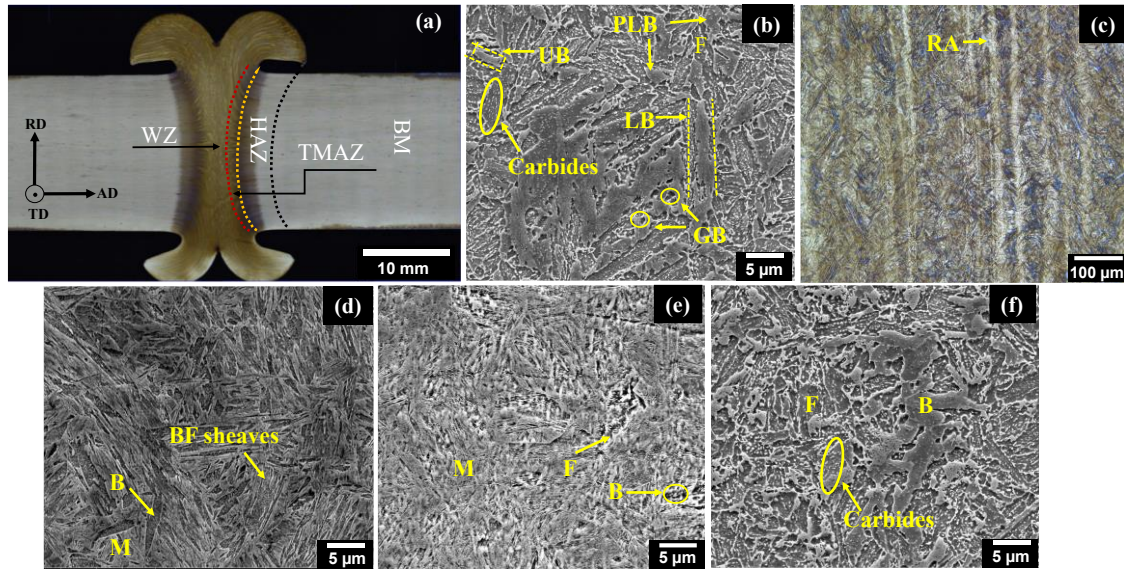


Fig. 2. SEM and OM micrographs of the BM and different regions of the weld (a) macro of the weld joint, (b) BM revealing the presence of different morphology of bainite, ferrite (F) and carbide precipitates; (c) and (d) OM and SEM micrographs of the WZ displaying the presence of bainitic ferrite (BF), martensite (M) and retained austenite (RA); (e) SEM micrograph of the TMAZ exhibiting the presence of ferrite (F), martensite (M), bainite (B), and (f) HAZ exhibiting similar microstructure as that of BM i.e. presence of bainite, ferrite and carbides.

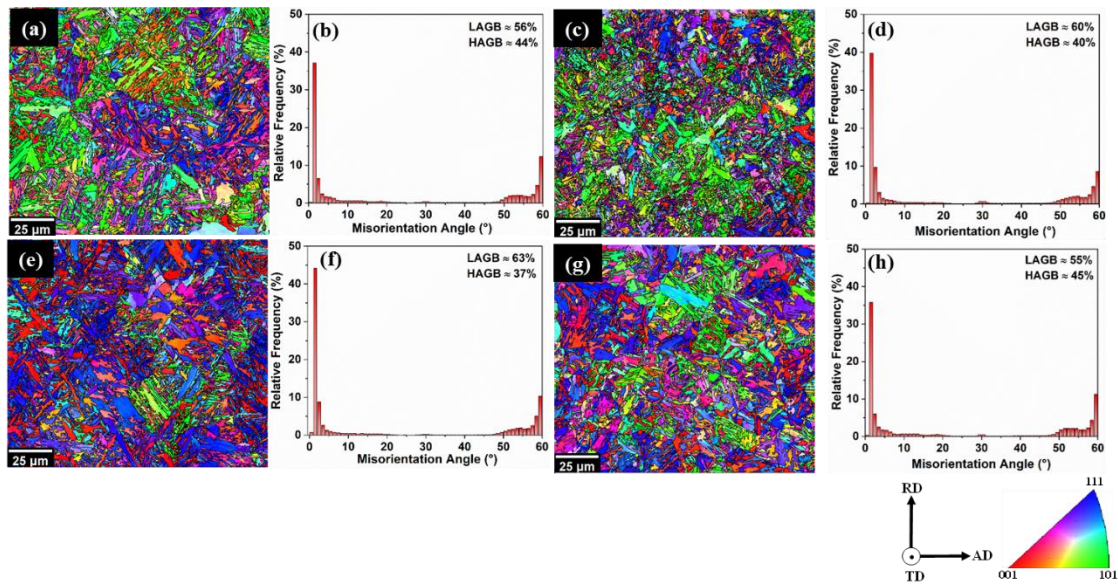
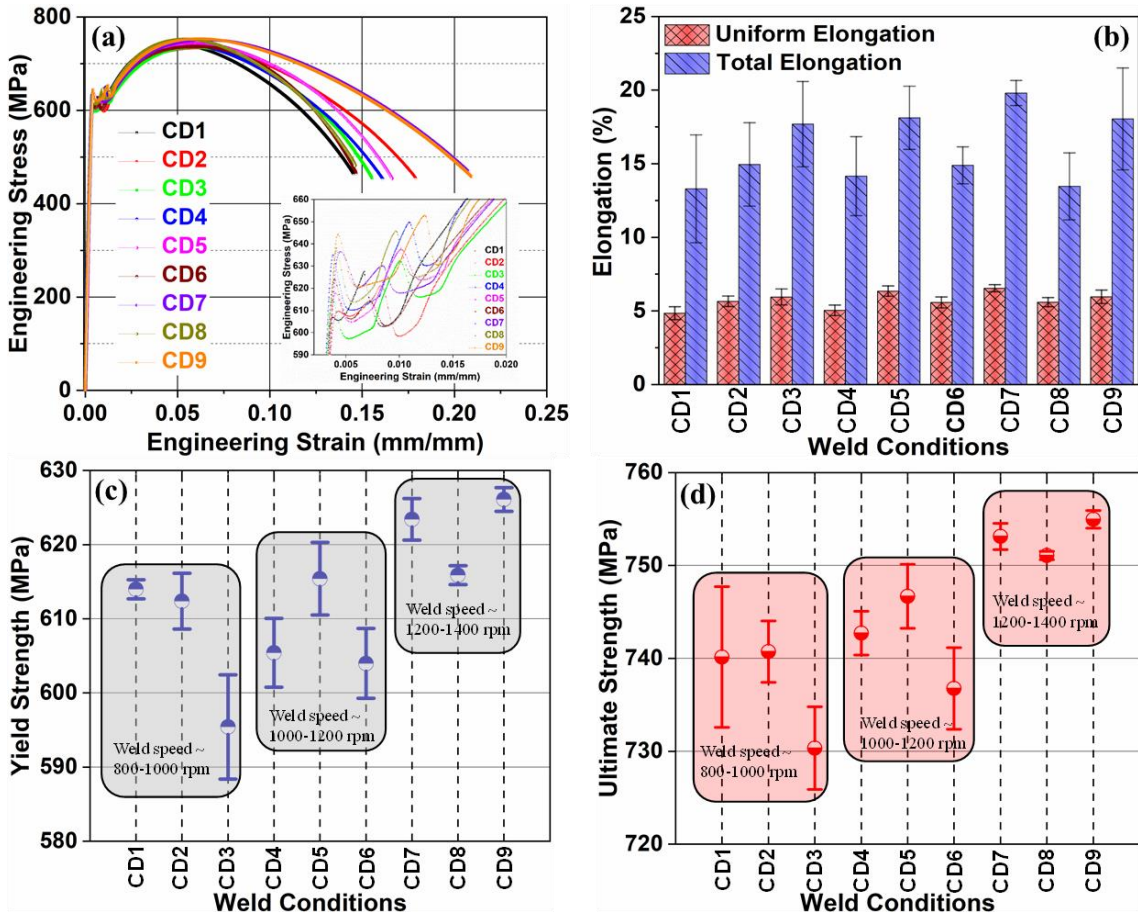


Fig. 3. OIMs with IPF colouring with respect to the AD, and plots of misorientation angle distribution for different regions of the CD9 weld, (a) BM, (b) WZ, (c) TMAZ and (d) HAZ. The RD, AD and TD represents the radial, axial and transverse directions.

555



556

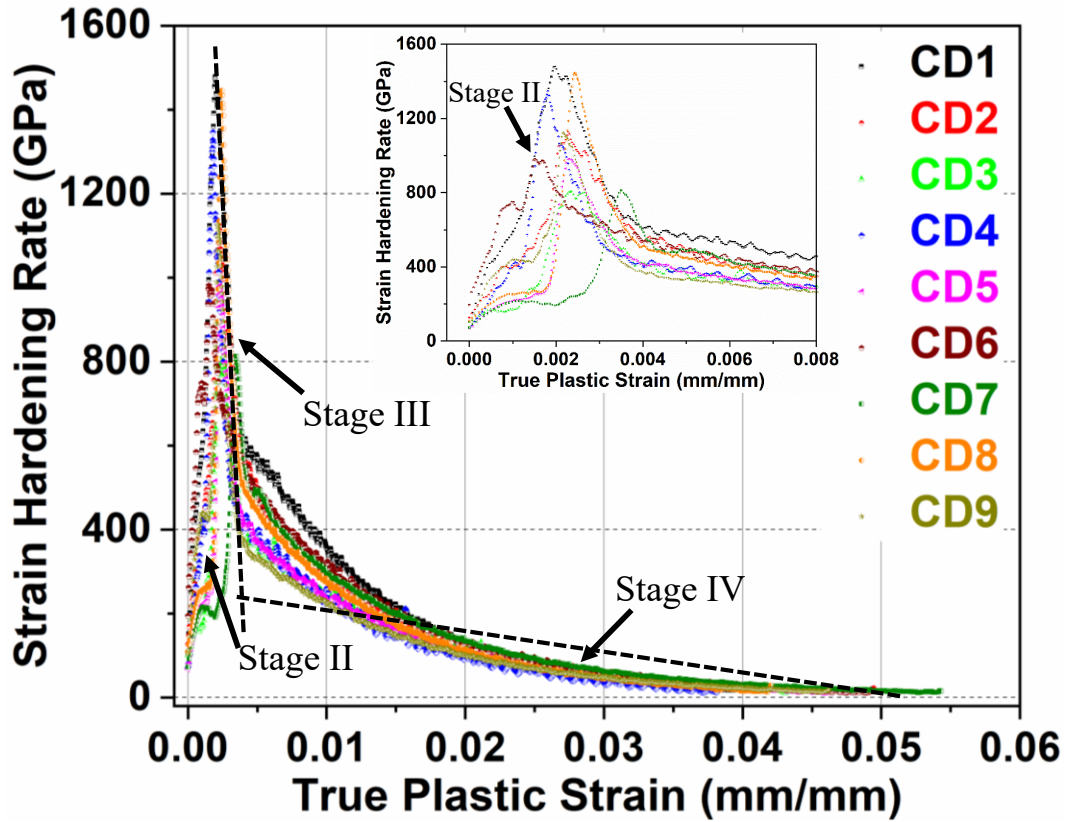
557

558

559

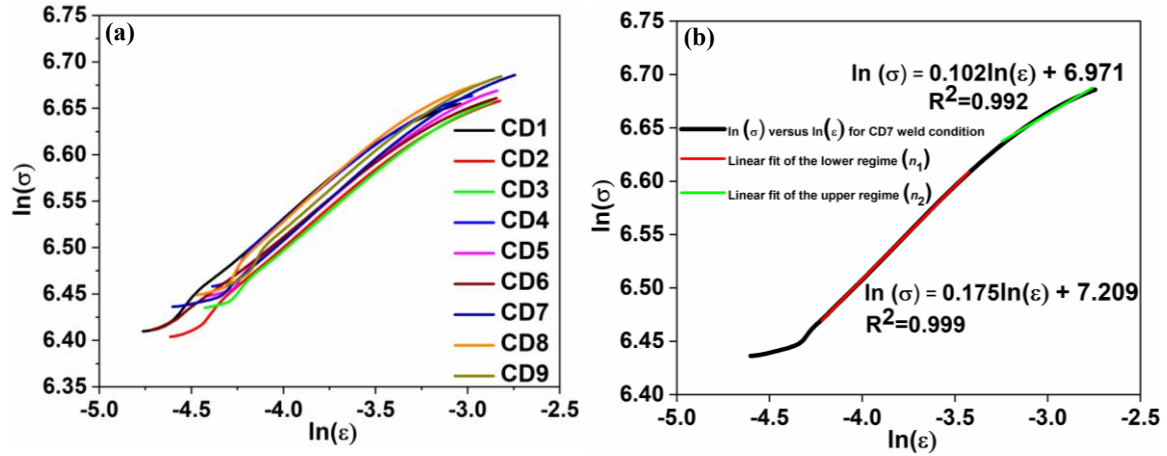
560

Fig. 4. (a) Engineering stress-strain curves for the welded materials and the magnified image in the inset showing the double yielding and yield point elongation during tensile tests for all samples, (b) uniform and total elongation, (c) and (d) show the variation in yield and UTS, respectively, as a function of rotation speed for different weld conditions.



561
562
563

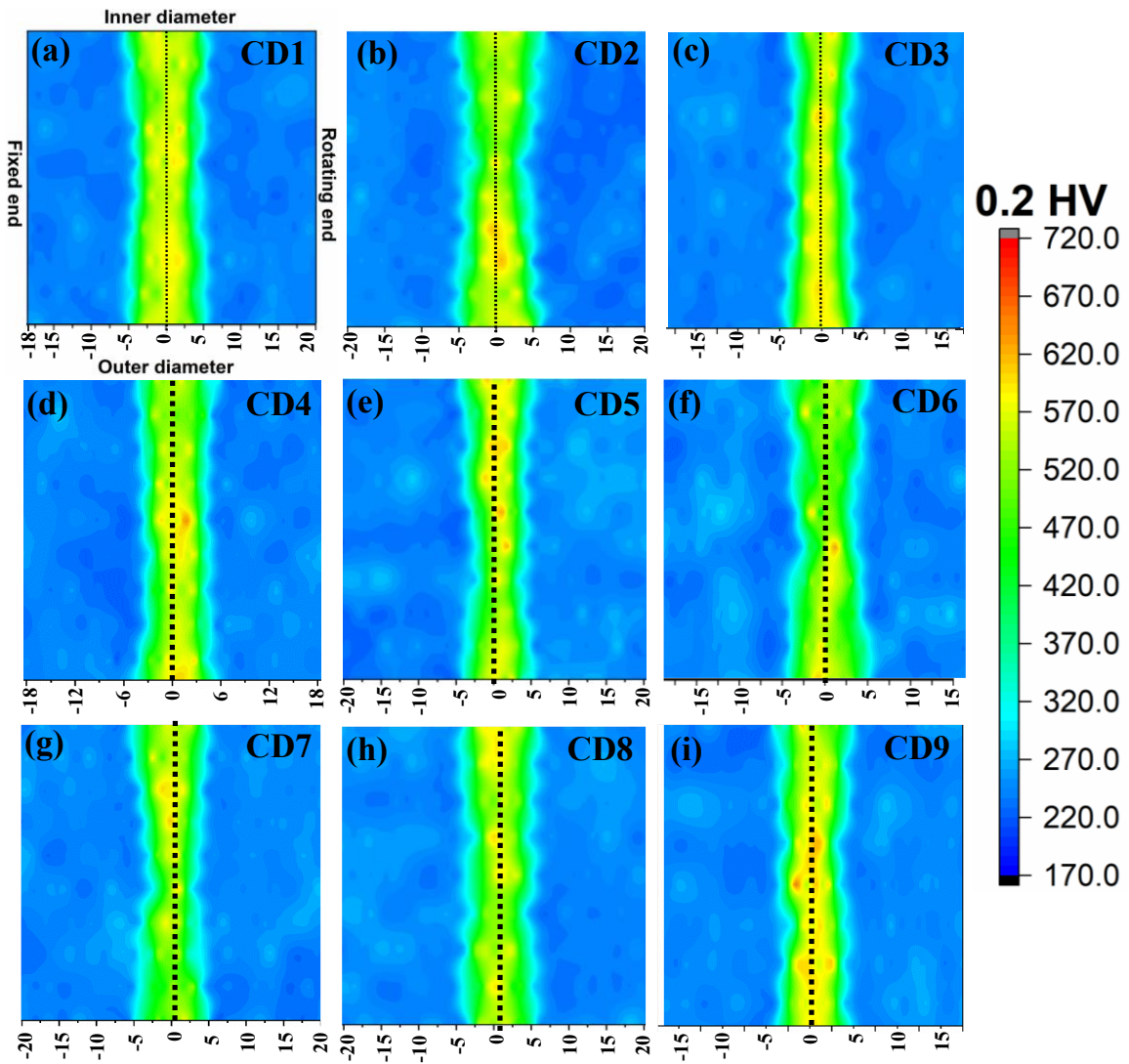
Fig. 5. The strain hardening rate versus true plastic strain of the welded samples exhibiting three different stages. Inset is the magnified plot exhibiting stage II.



564
565
566

Fig. 6. (a) Strain hardening behaviour of the welds exhibiting variations of $\ln \sigma$ vs $\ln \epsilon$, (b) methodology used for evaluating the strain-hardening exponents for CD 9 weld

567

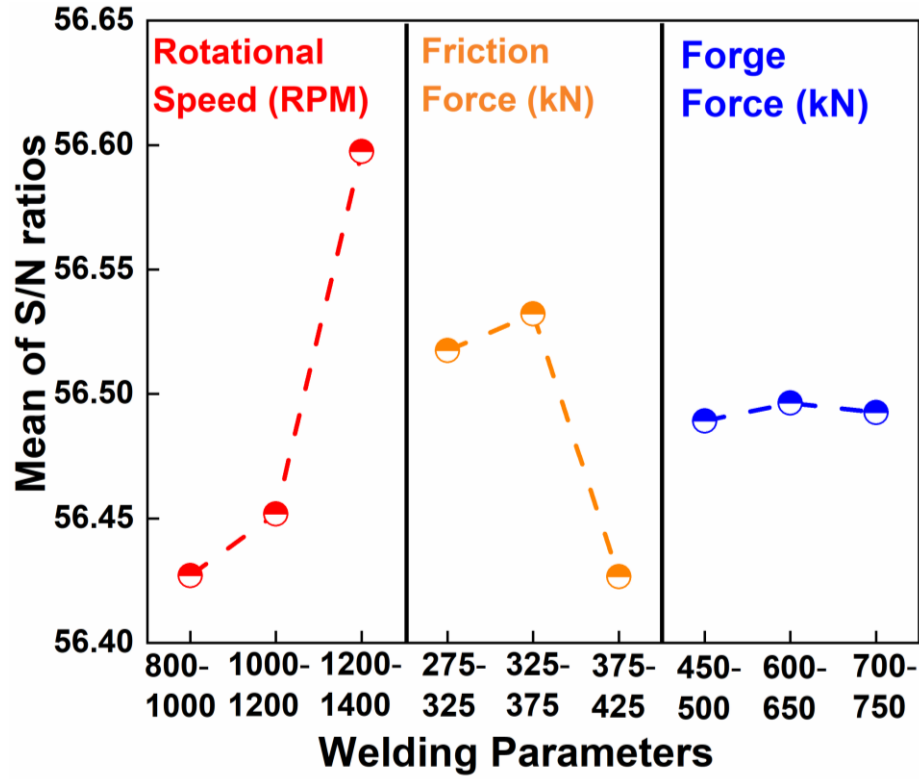


568

569

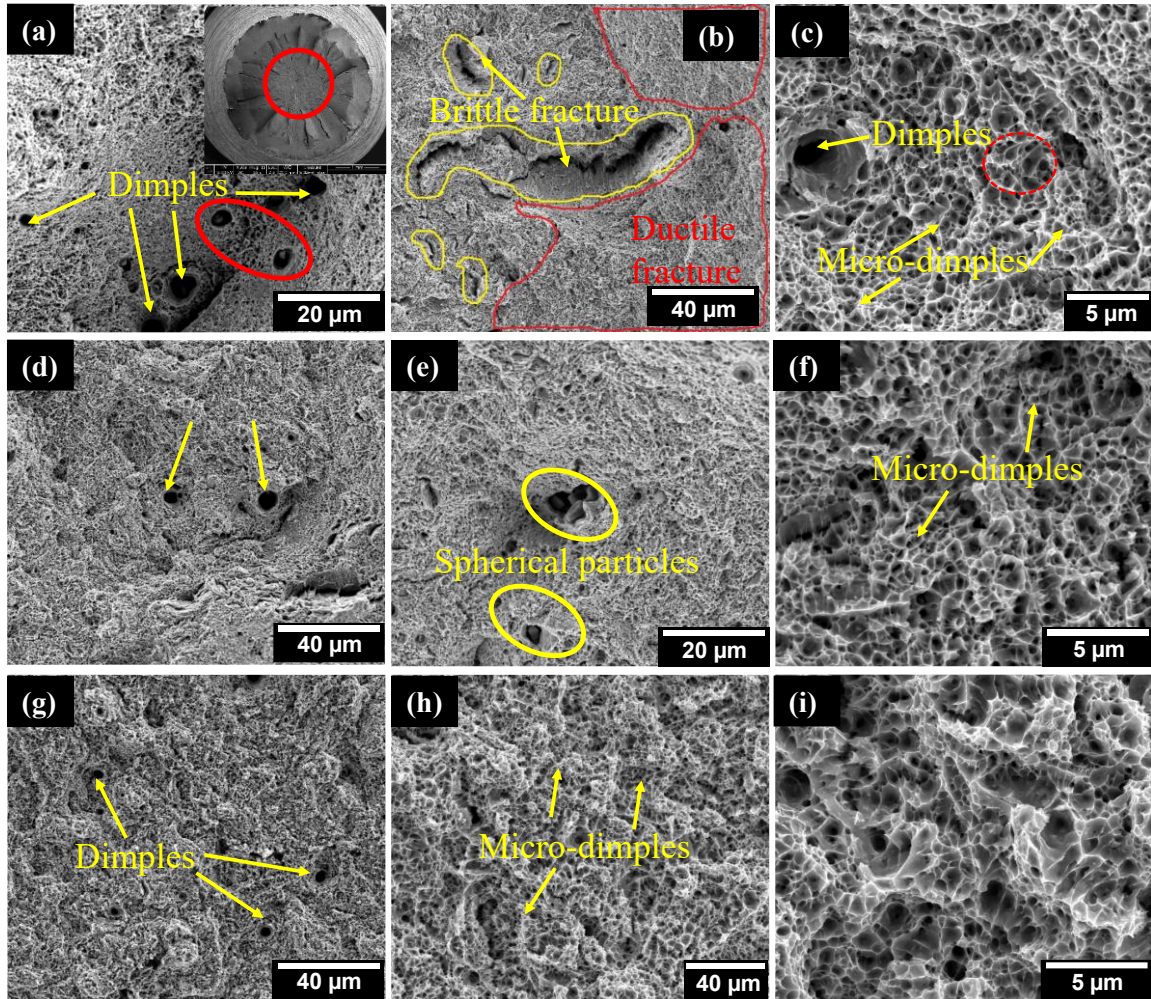
570

Fig. 7. Microhardness maps of all the nine CDW welds exhibiting the hardness distribution across the WZ, TMAZ, HAZ and BM.



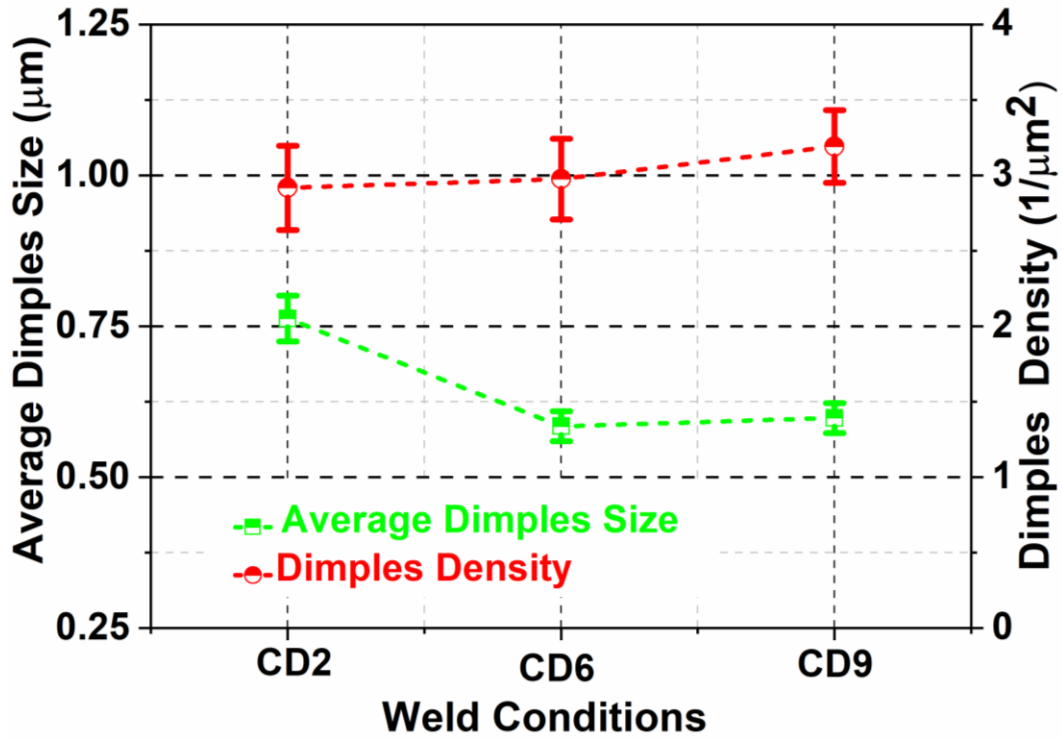
571

572 **Fig. 8.** ANOVA analysis exhibiting the effects of individual process parameters on the UTS
573 of the welds performed in this study.



574

575 **Fig. 9.** Fracture morphologies of the welds following tensile experiments, (a) - (c) CD2
 576 weld, (d) - (f) CD6 weld, (g) - (i) CD9 weld exhibiting the presence of various features such as dimples, micro-dimples, presence of spherical particles and macroscopic cracks.
 577



578

579 Fig. 10. Variation in the measured dimple size and density as a function of weld conditions.

580

Tables

581 **Table 1.** The identity and ranges of RFW process parameters implemented during CDW in
582 this study.

Specimen	Rotational speed (RPM)	Friction force (kN)	Forge force (kN)
CD1	800 - 1000	275 - 325	450 – 500
CD2	800 - 1000	325 - 375	600 - 650
CD3	800 - 1000	375 - 425	700 - 750
CD4	1000 - 1200	275 - 325	600 - 650
CD5	1000 - 1200	325 - 375	700 - 750
CD6	1000 - 1200	375 - 425	450 - 500
CD7	1200 - 1400	275 - 325	700 - 750
CD8	1200 - 1400	325 - 375	450 - 500
CD9	1200 - 1400	375 - 425	600 - 650

583

584 **Table 2.** Strain hardening exponents and hardening capacity for the BM and the welds

Condition	n_1	n_2	H_c
BM	0.336	0.187	0.280
CD1	0.172	0.088	0.205 \pm 0.004
CD2	0.169	0.092	0.209 \pm 0.007
CD3	0.167	0.105	0.227 \pm 0.001
CD4	0.165	0.095	0.226 \pm 0.005
CD5	0.165	0.094	0.213 \pm 0.004
CD6	0.159	0.093	0.220 \pm 0.002
CD7	0.175	0.102	0.208 \pm 0.005
CD8	0.177	0.095	0.219 \pm 0.002
CD9	0.170	0.101	0.214 \pm 0.004

585

586 **Table 3.** Maximum hardness values obtained for the WZ of all the welds produced under
587 different conditions.

Welds	CD1	CD2	CD3	CD4	CD5	CD6	CD7	CD8	CD9
Maximum HV	693	686	699	683	702	716	683	661	673

588

589 **Table 4.** Summary of the calculated values for the ANOVA parameters

Source	Degree of freedom	Sum of squares	Mean of squares	F-test	P-test	Contribution (%)
Rotational speed	2	303.69	151.84	2.99	0.251	59.66
Friction force	2	103.08	51.54	1.01	0.496	20.25
Forge force	2	0.685	0.342	0.01	0.993	0.13
Residual error	2	101.57	50.78			19.95
Total	8	509.02				100

590

